Optics Letters

Time-domain diffuse optics with 8.6 mm² fast-gated SiPM for extreme light harvesting

L. Di Sieno,[1,*,†] E. Ferocino,[1,†] E. Conca,[2] V. Sesta,[2] M. Buttafava,[2] F. Villa,[2] F. Zappa,[2] D. Contini,[1] A. Torricelli,[1,3] P. Taroni,[1,3] A. Tosi,[2] A. Pifferi,[1,3] and A. Dalla Mora[1]

[1] *Politecnico di Milano, Dipartimento di Fisica, 20133 Milano, Italy*
[2] *Politecnico di Milano, Dipartimento di Elettronica, Informazione e Bioingegneria, 20133 Milano, Italy*
[3] *Consiglio Nazionale delle Ricerche, Istituto di Fotonica e Nanotecnologie, 20133 Milano, Italy*
*Corresponding author: laura.disieno@polimi.it

Fast time-gated single-photon detectors demonstrated high depth sensitivity in the detection of localized absorption perturbations inside scattering media, but their use for *in vivo* clinical applications—such as functional imaging of brain activation—was impaired by their small (<0.04 mm²) active area. Here, we demonstrate, both on phantoms and *in vivo*, the performance of a fast-gated digital silicon photomultiplier (SiPM) that features an overall active area of 8.6 mm², overcoming the photon collection capability of established time-gated single-pixel detectors by orders of magnitude, enabling deep investigations within scattering media and high signal-to-noise ratios at late photon arrival times. © 2021 Optical Society of America under the terms of the OSA Open Access Publishing Agreement

https://doi.org/10.1364/OL.413577

Highly scattering media (e.g., biological tissues) can be probed in depth using visible or near-infrared light [1]. Among different approaches, time-domain diffuse optics (TDDO) permits high depth sensitivity and selectivity even in reflectance geometry (i.e., light injection and collection on the same side) [2]. Further, depth sensitivity can be increased by reducing the source-detector separation (SDS) as, in TDDO, the average depth probed by photons depends only on their traveling time [3]. Therefore, late-arriving photons carry information about deeper regions within the investigated medium.

The adoption of a short SDS permits us to increase the intensity of collected light at all photon arrival times, but, for early photons, this gain can overcome that of late photons by orders of magnitude [4], requiring a time-gated detection scheme to avoid the saturation of the detection chain [5]. While in ideal conditions [i.e., with a Dirac-delta instrument response function (IRF)] the null SDS yields the best measurement results [4], the IRF shape of real systems leads to performance degradation, thus resulting in an optimum value of the SDS of >1 cm, depending on specific IRF contributions (such as photon times spread, e.g., due to decaying tails [6] and memory effect [7]), detector area, and many other system characteristics [8].

Time-gated detectors with sub-nanosecond (ns) switching time have been demonstrated using single-photon avalanche diodes (SPADs) [5]. However, potential increase in the signal given by the use of a short SDS has been largely hindered by their tiny active areas (diameters ranging from 10 to 200 μm) [9,10] with respect to photomultiplier tubes (PMTs) (representing the classical choice for TDDO). For this reason, time-gated TDDO has been used for different proof of concept studies [5], without resulting in widespread adoption.

In a previous work [11], the design and electrical characterization of a new class of photodetectors for TDDO was introduced [namely, fast-gated digital silicon photomultiplier (FG-dSiPM)], featuring both sub-ns gating capability and a wide active area (>8 mm²), thanks to the parallelization of 1728 SPAD pairs (i.e., pixels) on a single digital chip, which can be separately enabled or disabled to tune the light harvesting efficiency. Each SPAD has a square footprint with about 50 μm side and rounded corners. Avoiding saturation, 32 pixels out of the 1728 are covered by a circular pinhole (8 with 5, 10, 20, 40 μm pinhole diameters) in order to extend the possibility of also using the detector at high photon fluxes. Its performances in TDDO were not fully demonstrated yet.

In this work, the FG-dSiPM is validated in a laboratory setting on tissue-mimicking phantoms relying on a few selected internationally agreed upon figures of merit defined by established and rigorous protocols for performance assessment of diffuse optics systems [12,13]. Further, a preliminary *in vivo* validation is shown in the detection of the functional brain activation of three subjects performing a finger tapping exercise. This accomplishment overcomes a bottleneck in TDDO—namely, the tiny area —thus opening up perspectives for more sensitive, wearable, or hand-held devices.

A pulsed driver coupled to a 670 nm laser head (PDL 828 Sepia II and LDH P C 670M, Picoquant GmbH, Germany) provided light pulses at 40 MHz repetition rate. Light was fiber-coupled (step index, 600 μm core) after passing through a variable optical attenuator (VOA), thus allowing the selection of the desired photon counting rate (the maximum average power at the sample was 5.5 mW). The printed circuit board of the FG-dSiPM (whose dimensions are 120 mm × 60 mm × 22 mm)

was directly hosted into a flexible black neoprene probe together with the laser injection fiber at 2.5 cm SDS (distance between the detector and optical fiber core centers). The output pulse in response to single-photon detection was fed to a time-correlated single-photon counting (TCSPC) board (SPC130, Becker and Hickl GmbH, Germany). A custom-made voltage pulser was employed to provide trigger signals to the laser, the FG-dSiPM detector, and the synchronization signal to the TCSPC board.

The IRF was measured by directly coupling the source fiber with the detector, with a thin (100 μm) Teflon layer in between to provide quasi-isotropic illumination [12]. The time-gated acquisition technique, i.e., acquisition of different slices of the optical waveform under measurement by setting for each one the targeted photon counting rate using the VOA, followed by post-processing reconstruction by rescaling the amplitude of each slice for the employed attenuation [5], was used to extend the detector dynamic range. In detail, about 120 slices were acquired (each one for 5 s of integration time) in 50 ps steps. The IRF shape was measured for different sizes of the enabled area.

Among different reconstructed IRFs, three representative cases are shown in Fig. 1 (left), reporting the response in case of activation of (i) a single pixel with the smallest pinhole size (5 μm), (ii) a single pixel without a pinhole (50 μm), and (iii) 1708 pixels [i.e., all pixels that can be tuned ON, including those with pinholes, but excluding 20 pixels with the highest dark count rate, i.e., higher than 32,000 counts per second (cps)]. For comparison, the contribution of the detector response to the IRF can be found in Conca _et al._ [11]. Other combinations have been omitted from the picture for clarity, but do not exhibit relevant differences. For all measured combinations, the first tail of the temporal response decays by ~4 orders of magnitude in ~2 ns, while the second decay tail (i.e., the so-called memory effect [7]) clamps the IRF dynamic range to ~5 orders of magnitude. State-of-the-art fast-gated SPADs [14] typically exhibit better temporal responses (e.g., the first tail decays by >4 orders of magnitude in 1 ns, and the memory effect clamps the dynamic range at about 5–8 orders of magnitude, depending on the wavelength of excitation), but the maximum diameter ever demonstrated for fast-gated SPADs is 200 μm [15], thus resulting into an area of 0.031 mm^2 instead of the 8.6 mm^2 achieved here with 1708 pixels.

Reference [12] introduced a measurement procedure to evaluate the overall diffused light harvesting efficiency (namely "responsivity" in the field of TDDO). Figure 1 (right) shows this figure of merit as a function of the size of the enabled area from the smallest pixel to all 1708 pixels.

The maximum responsivity measured here is 1.74×10^{-6} m^{2}sr, thus reaching values about 5 orders of magnitude higher than fiber-based gated SPADs [14] and about 2 orders of magnitude higher than probe-hosted SPADs [15]. If compared with our exemplary (not gated) TDDO system, with light collection based on 3 mm core fiber bundles and hybrid PMTs [16], responsivity is still 40 times higher.

As dictated by [12], the instrument warm-up and stability were assessed in terms of IRF counts, shape, and barycenter over 3 h of continuously repeated measurements with the laser pulse peak set inside the gating window (10 ns width) of the detector, resulting in all of the performances being in line with state-of-the-art devices. In particular, Fig. 2 shows the photon count warm up for minimum (1 pixel ON with a standard count rate of ~1 Mcps) and high (1708 pixels ON with a high count rate of ~3 Mcps) power dissipation cases. In both cases, after ~ 20 min, the stability is reached (i.e., counts stay between dotted lines for hours).

The performance in detecting deep absorption perturbations was studied on phantoms following the procedures defined in [13]. A tissue-mimicking (absorption $\mu_a = 0.1$ cm^{-1}, reduced scattering $\mu_s' = 10$ cm^{-1} at 670 nm) liquid phantom was prepared using a calibrated mixture of water, Intralipid, and India ink. The phantom was hosted inside a black polyvinyl chloride (PVC) tank [13] with a lateral window sealed by a thin Mylar foil, allowing optical access for the probe. A totally absorbing PVC cylindrical object with a volume of about 100 mm^3 (height = diameter = 5 mm) was set at different depths inside the phantom with respect to the probe. As demonstrated in [17], this perturbation is equivalent to a realistic absorption perturbation featuring $\Delta\mu_a = 0.16$ cm^{-1} in 1 cm^3 volume. The perturbation was scanned along a direction orthogonal to the probe inside the phantom, starting from a depth of its center of 2.5 mm (i.e., perturbation edge touching the Mylar foil in the middle between the center of the optical fiber and the center of the detector) up to 50 mm in 2.5 mm steps. For each position, a reference homogeneous measurement was taken (i.e., perturbation at 55 mm depth, where its effect is negligible). The measurement was repeated for different sizes of enabled active areas, chosen among those plotted in Fig. 1 (right) so as to approach steps of about 1 order of magnitude in responsivity. For each area, the FG-dSiPM gating window (7 ns
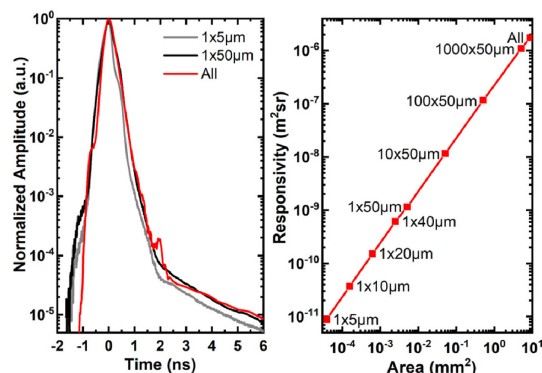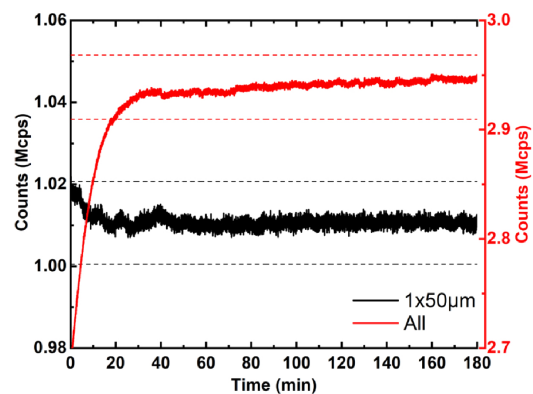

Fig. 1. (Left) IRFs at different detection area sizes (i.e., pixel combinations) and (right) responsivity dependence on enabled area (number of pixels and pixel area are reported for each data point).

Fig. 2. IRF counts variations due to warm-up: 1 pixel ON and standard count rate of ~ 1 Mcps (black line) and 1708 pixels ON and high count rate of ~ 3 Mcps (red line). The dotted lines represent the ±1% variation computed on the average value of counts after 20 min.

width) was set at the latest delay with respect to the IRF peak position that allowed a photon counting rate of 1 Mcps with full laser power (VOA set as fully open). For each depth and area, two figures of merits were computed [13]: (*i*) contrast (*C*), with $C = (N_0 - N)/N_0$, where N_0 and N are the number of counts inside a given temporal window along the recorded distribution of photons time-of-flight in the TCSPC histogram, respectively, in the unperturbed and perturbed cases; (*ii*) contrast-to-noise ratio (CNR), with $\mathrm{CNR} = (N_0 - N)/\sigma(N_0)$, where $\sigma(N_0)$ is the standard deviation of the number of counts for the unperturbed case. To enable the calculation of the CNR, each acquisition (1 s) was therefore repeated five times to estimate count fluctuations. For all of the acquisitions, the best positions for the temporal window (400 ps width) used to compute *C* and CNR were chosen as the best compromise between depth penetration and CNR values. As in TDDO, the photon arrival times encode the average penetration; this criterion allows us to simultaneously report advantages in terms of both CNR and penetration in the medium.

Results are presented in Fig. 3, where the bottom limit of the *y* axis was limited to 1% for *C* (left) and one for CNR (right), usually considered as the threshold limits for detectability of perturbations inside biological tissues [15]. For clarity, points featuring *C* > 1% with corresponding CNR < 1 have been removed from the left plot, being dominated by noise. It is clear that wide areas permit us to increase the CNR at all depths of the perturbation thanks to the increase in the signal level allowed by the extreme light harvesting efficiency. With larger areas, it is possible to compute *C* at later delays with respect to the IRF peak, thus probing deeper regions. Therefore, upon increasing the detector area, the *C* function increases at deeper positions of perturbation. Eventually, in this system, the detector allowed us to reach the remarkable depth of investigation of 37.5 mm if considering both limits on *C* and CNR, while the CNR exceeds one up to 42.5 mm. For the sake of comparison, the 200 µm diameter probe-hosted fast-gated SPAD introduced in [15] permitted us to detect the same perturbation up to a depth of only 25 mm. The 100 µm diameter fiber-based fast-gated SPAD presented in [14] was instead limited to 16 mm due to the much lower responsivity resulting from the combination of a smaller active area and the limited numerical aperture of fiber-based detection. Only if combined with a high power laser (~100 mW) [18] did this 100 µm detector allow us to sense the perturbation down to a depth of 30 mm. With the system
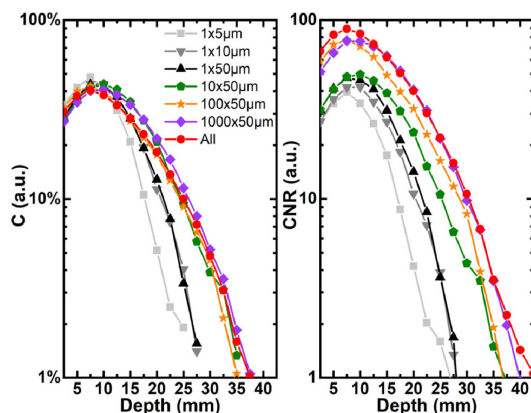

Fig. 3. *C* (left) and CNR (right) produced by a perturbation equivalent to $\Delta\mu_a = 0.16\ \mathrm{cm}^{-1}$ set at various depths inside the liquid phantom at different sizes of enabled detector area (colors).

presented here, it was possible to probe about 1 cm deeper than any other gated system presented before, and the combination with high power lasers can further push this limit in the future.

As a preliminary *in vivo* validation, the system was tested in the detection of the localized brain activity on three right-handed healthy volunteers during a finger tapping experiment (Subject 1: male, 51 years old (y.o.), bald; Subject 2: male, 39 y.o., with dark hair about 1 cm long; Subject 3: male, 55 y. o., with pale hair about 1 cm long). The protocol was approved by the Ethical Committee of Politecnico di Milano and was conducted in agreement with the Declaration of Helsinki. A written informed consent was given by all subjects before participation.

The probe was placed on the left motor cortex area, with the C3 position of the international 10–20 reference system for electrodes placement positioned between the center of the source fiber and the center of the detector. The protocol consisted of five repetitions of the following sequence: 20 s of baseline followed by 20 s of finger tapping (self-paced, with finger opposition) and finally 20 s for recovery. It was performed first with the right hand and then repeated with the left hand. For each subject, similarly to the phantom study, the FG-dSiPM gating window (7 ns width) was set at the latest delay with respect to the IRF peak position that permitted us to achieve a photon counting rate of 1 Mcps with full laser power (VOA fully open). This choice allows one to optimize the contrast on each subject, which will be otherwise limited by Subject 2 due to his dark hair. Acquisitions were continuously taken at 1 Hz rate. The *C* during the task produced by task-related hemodynamic changes was computed inside a 400 ps window set at a delay along the acquired distribution of photons time-of-flight that maximizes the number of photon counts considered, thus minimizing the Poisson noise contribution during the analysis. This criterion is different with respect to phantom measurements, since *in vivo* measurements do not allow one to trade off between C and CNR, as repeated measurements are in that case affected by biological variations.

The reference case for the computation of *C* was taken from the average of the five repetitions acquired during the baseline phase of the protocol (from 5 s to 10 s). The use of a single wavelength does not allow one to disentangle contributions of oxygenated and deoxygenated hemoglobin (O_2Hb, HHb). However, at a 670 nm wavelength, the main tissue absorber is HHb. During the task, as a result of the neurovascular coupling, HHb is expected to decrease, while O_2Hb and the total amount of blood are expected to increase. As the sensitivity of the system at this wavelength is much higher for HHb, an activation will produce an increase in the total amount of photon counts with respect to the baseline and thus a decrease in *C*.

Figure 4 shows the results for *C* (folding average of five repetitions) for both hands of all subjects. The standard deviation of *C* over the five repetitions is represented by vertical error bars. It is worth noting that the standard deviation is not only due to electronic noise and drifts, as otherwise the stability measurement in Fig. 2 should show higher variability, but most probably due to biological fluctuations like systemic hemodynamic changes occurring in the scalp or background brain processes (in addition to the activation governing the finger tapping exercise) in the probed region. As shown, there is a clear task-related contralateral activation for both Subjects 1 and 3. The same activation is also detectable for Subject 2, but it is more confounded by noise. This was expected, as the measurement on Subject 2 was
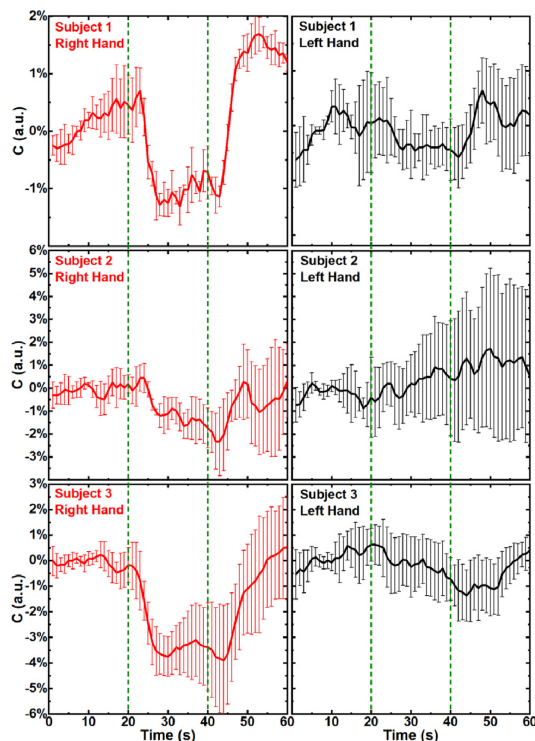
Fig. 4. *C* (folded average of five repetitions) during the motor protocol (finger tapping) for the three subjects (rows). Results are shown for the exercise performed with either right or left hand (columns).

performed by opening the gating window of the FG-dSiPM at a delay of just ∼1.3 ns with respect to the IRF peak, while this delay was set to ∼3.6 ns on Subject 1 and ∼2.3 ns on Subject 3. This shorter delay on Subject 2 is due to the stronger attenuation (most probably due to the presence of dark hair) that prevented the use of longer delays, thus probing shallower regions of the head structure and, most probably, just approaching the brain motor cortex. Subject 1 was instead bald, thus permitting much longer delays of investigation. However, Subject 1 exhibits the faintest C variation among the three subjects, most probably due to the longest delay of the FG-dSiPM window causing a strong contamination by the memory effect of the detector [6,7]. Subject 1 also exhibits a weak ipsilateral activation, probably due to a faint task-related systemic activity.

In summary, the first fast time-gated digital silicon photomultiplier (FG-dSiPM) featuring a wide active area of about 8.6 mm^2 has been characterized and validated on phantoms and *in vivo* for TDDO, demonstrating performances well beyond all other state-of-the-art microelectronic-gated detectors in this application. The overall light harvesting efficiency was 2–5 orders of magnitude higher than that of gated SPADs, a feature that permits us to reach the remarkable depth of investigation of 37.5 mm inside a liquid phantom with realistic optical properties, overcoming the maximum investigated depth of all other fast-gated detectors previously validated for TDDO applications. Preliminary *in vivo* investigations have also demonstrated its suitability in following hemodynamic changes. As discussed in [11], this detector was designed to target the future fabrication of portable and wearable time-gated TDDO systems. Together with the recent development of miniaturized pulsed laser sources [9,19], this work can open the way to a new class

of TDDO systems, permitting the fabrication of fully operative optodes with a level of compactness close to wearable continuous-wave diffuse optics devices, but with superior performances. In years to come, this can push a widespread use of this technology in different scenarios, from medical imaging applications (e.g., brain monitoring or cancer diagnostics) to the consumer level (e.g., personal healthcare monitoring or muscular oxygenation monitoring for sportsmen).

REFERENCES

1. A. Yodh and B. Chance, Phys. Today **48**(3), 34 (1995).
2. A. Pifferi, D. Contini, A. Dalla Mora, A. Farina, L. Spinelli, and A. Torricelli, J. Biomed. Opt. **21**, 091310 (2016).
3. S. Del Bianco, F. Martelli, and G. Zaccanti, Phys. Med. Biol. **47**, 4131 (2002).
4. A. Torricelli, A. Pifferi, L. Spinelli, R. Cubeddu, F. Martelli, S. Del Bianco, and G. Zaccanti, Phys. Rev. Lett. **95**, 078101 (2005).
5. A. D. Mora, L. Di Sieno, R. Re, A. Pifferi, and D. Contini, Appl. Sci. **10**, 1101 (2020).
6. D. Contini, A. D. Mora, L. Spinelli, A. Farina, A. Torricelli, R. Cubeddu, F. Martelli, G. Zaccanti, A. Tosi, G. Boso, F. Zappa, and A. Pifferi, J. Phys. D **48**, 045401 (2015).
7. A. D. Mora, A. Tosi, D. Contini, L. Di Sieno, G. Boso, F. Villa, and A. Pifferi, J. Appl. Phys. **117**, 114501 (2015).
8. A. Behera, L. Di Sieno, A. Pifferi, F. Martelli, and A. D. Mora, Biomed. Opt. Express **9**, 5524 (2018).
9. S. Saha, Y. Lu, S. Weyers, M. Sawan, and F. Lesage, IEEE Photon. Technol. Lett. **30**, 1515 (2018).
10. M. Alayed and M. J. Deen, Sensors **17**, 2115 (2017).
11. E. Conca, V. Sesta, M. Buttafava, F. Villa, L. Di Sieno, A. D. Mora, D. Contini, P. Taroni, A. Torricelli, A. Pifferi, F. Zappa, and A. Tosi, IEEE J. Solid-State Circuits **55**, 3097 (2020).
12. H. Wabnitz, D. R. Taubert, M. Mazurenka, O. Steinkellner, A. Jelzow, R. Macdonald, D. Milej, P. Sawosz, M. Kacprzak, A. Liebert, R. Cooper, J. Hebden, A. Pifferi, A. Farina, I. Bargigia, D. Contini, M. Caffini, L. Zucchelli, L. Spinelli, R. Cubeddu, and A. Torricelli, J. Biomed. Opt. **19**, 086010 (2014).
13. H. Wabnitz, A. Jelzow, M. Mazurenka, O. Steinkellner, R. Macdonald, D. Milej, N. Żołek, M. Kacprzak, P. Sawosz, R. Maniewski, A. Liebert, S. Magazov, J. Hebden, F. Martelli, P. Di Ninni, G. Zaccanti, A. Torricelli, D. Contini, R. Re, L. Zucchelli, L. Spinelli, R. Cubeddu, and A. Pifferi, J. Biomed. Opt. **19**, 086012 (2014).
14. L. Di Sieno, H. Wabnitz, A. Pifferi, M. Mazurenka, Y. Hoshi, A. D. Mora, D. Contini, G. Boso, W. Becker, F. Martelli, A. Tosi, and R. Macdonald, Rev. Sci. Instrum. **87**, 035118 (2016).
15. A. D. Mora, D. Contini, S. Arridge, F. Martelli, A. Tosi, G. Boso, A. Farina, T. Durduran, E. Martinenghi, A. Torricelli, and A. Pifferi, Biomed. Opt. Express **6**, 1749 (2015).
16. R. Re, D. Contini, M. Turola, L. Spinelli, L. Zucchelli, M. Caffini, R. Cubeddu, and A. Torricelli, Biomed. Opt. Express **4**, 2231 (2013).
17. F. Martelli, A. Pifferi, D. Contini, L. Spinelli, A. Torricelli, H. Wabnitz, R. Macdonald, A. Sassaroli, and G. Zaccanti, J. Biomed. Opt. **18**, 066014 (2013).
18. L. Di Sieno, A. D. Mora, A. Torricelli, L. Spinelli, R. Re, A. Pifferi, and D. Contini, Appl. Sci. **9**, 2366 (2019).
19. L. Di Sieno, J. Nissinen, L. Hallman, E. Martinenghi, D. Contini, A. Pifferi, J. Kostamovaara, and A. D. Mora, J. Biomed. Opt. **22**, 085004 (2017).